

Effect of substitution La by Mg on electrochemical and electronic properties in $\text{La}_{2-x}\text{Mg}_x\text{Ni}_7$ alloys: a combined experimental and *ab initio* studies

Mirosław Werwiński*, Andrzej Szajek, Agnieszka Marczyńska, Lesław Smardz

*Institute of Molecular Physics, Polish Academy of Sciences,
M. Smoluchowskiego 17, 60-179 Poznań, Poland*

Marek Nowak, Mieczysław Jurczyk

*Institute of Materials Science and Engineering, Poznań University of Technology,
Jana Pawła II No. 24, 61-138 Poznań, Poland*

arXiv:2503.14952v1 [cond-mat.mtrl-sci] 19 Mar 2025

Abstract

La-Mg-Ni-based alloys are promising negative electrode materials for 3rd generation of Ni-MH_x batteries. In this work we investigate the effect of Mg substitution on the electrochemical and electronic properties of $\text{La}_{2-x}\text{Mg}_x\text{Ni}_7$ materials. The mechanical alloying technique is used to produce a series of $\text{La}_{2-x}\text{Mg}_x\text{Ni}_7$ alloys ($x = 0.00, 0.25, 0.50$ and 0.75). The X-ray diffraction measurements indicates multi-phase character of the samples with majority $(\text{La},\text{Mg})_2\text{Ni}_7$ phases of hexagonal Ce_2Ni_7 -type and rhombohedral Gd_2Co_7 -type. Electrochemical measurements show how the maximum discharge capacity (C_{max}) increases with Mg concentration and that reach the highest value of 304 mAh/g for $\text{La}_{1.5}\text{Mg}_{0.5}\text{Ni}_7$ ($x = 0.5$). The experimental efforts are followed by the density functional theory (DFT) calculations performed with the full-potential local-orbital minimum-basis scheme (FPLO). To simulate chemical disorder we use the coherent potential approximation (CPA). The calculations are focused on the $\text{La}_{1.5}\text{Mg}_{0.5}\text{Ni}_7$ composition with the highest measured value of C_{max} . Additionally, several other structures is considered as reference points. We find that hexagonal and rhombohedral structures of La_2Ni_7 have almost identical total energies which is in a good agreement with a coexistence of both phases in the samples. The calculated site preferences of Mg in both Ce_2Ni_7 -type and Gd_2Co_7 -type $\text{La}_{1.5}\text{Mg}_{0.5}\text{Ni}_7$ phases are consistent with the previous experimental data. Furthermore, the valence band of the nanocrystalline $\text{La}_{1.5}\text{Mg}_{0.5}\text{Ni}_7$ sample is investigated by X-ray photoelectron spectroscopy (XPS). The experimental XPS are interpreted based on the corresponding spectra calculated with DFT.

1. Introduction

Metal hydrides (MH_x) are one of the most important alternatives for hydrogen storage applications and have a big potential to solve several energy and environmental issues [1]. Metal hydrides can reversibly absorb and desorb hydrogen at ambient pressure and temperature. The microcrystalline hydride materials are conventionally prepared by arc or induction melting and subsequent annealing. The hydriding-dehydriding properties of metal hydrides can be improved by introduction of metastable phases and formation of nanocrystalline structures. It can be achieved through the application of a non-equilibrium processing technique, like for example mechanical alloying (MA) [2, 3]. From a perspective of industrial application, an important advantage of the MA process is the fact that the MA allows for production of large quantities of the material, keeping relatively low costs.

The recently investigated metal hydrides are the ternary microcrystalline compounds $(\text{RE-Mg})_2\text{Ni}_7$ (RE = rare-earth metals) [4, 5, 6, 7, 8]. Their hydrogen storage properties proved to be better than the characteristics of the corresponding binary compounds AB_n ($2 \leq n \leq 5$) [4]. $(\text{RE-Mg})_2\text{Ni}_7$ alloys with La or Ce are characterized by high hydrogen capacity, moderate hydrogen equilibrium pressure and relatively inexpensive constituent elements. An open question remains the influence of Mg substitutions in place of RE on the structural, electrochemical and electronic characteristics of $(\text{RE-Mg})_2\text{Ni}_7$ alloys.

This work continues our previous research on La-Mg-Ni alloys and composites [9, 10, 11]. An objective of this study is to investigate the influence of Mg concentration on the electrochemical and electronic properties of $\text{La}_{2-x}\text{Mg}_x\text{Ni}_7$ materials. The series of $\text{La}_{2-x}\text{Mg}_x\text{Ni}_7$ alloys (with $x = 0.00, 0.25, 0.50$ and 0.75) is produced by the MA technique. The experimental efforts of materials preparation and characterization are followed by theoretical studies based on the density functional theory (DFT). The $(\text{La},\text{Mg})_2\text{Ni}_7$ systems have been investigated by DFT before. Crivello *et al.* [12] presented a systematic study

*Corresponding author

Email address: werwinski@ifmpan.poznan.pl (Mirosław Werwiński)

of every ordered configuration of $(\text{La},\text{Mg})_2\text{Ni}_7$ and several other La-Mg-Ni systems. Based on the calculated heats of formation Crivello *et al.* concluded that the stability of the $(\text{La},\text{Mg})_2\text{Ni}_7$ ternary system decrease with Mg substitution, wherein both rhombohedral (Gd_2Co_7 -type) and hexagonal (Ce_2Ni_7 -type) symmetries were considered. In the next paper Crivello *et al.* [6] present a systematic DFT study on distribution of hydrogen in La_2Ni_7 , Mg_2Ni_7 and $\text{La}_{1.5}\text{Mg}_{0.5}\text{Ni}_7$ hosts, however the calculations were limited to the Ce_2Ni_7 prototype. In both mentioned works the Mg alloying was modeled based on the ordered compound method. Furthermore, as the surveys focus on the systems stability, no results of valence band investigations were presented. The valence band of isostructural hexagonal La_2Co_7 has been shown before. [13]

2. Experimental and Computational Details

This sections covers the details of preparation of $\text{La}_{2-x}\text{Mg}_x\text{Ni}_7$ samples and reference elemental thin films. The applied characterization techniques, which are X-ray diffraction (XRD), X-ray photoelectron spectroscopy (XPS) and electrochemical measurements are also described. Finally, the computational parameters of *ab initio* calculations are given.

2.1. Materials Preparation

For preparation of the samples we used the La powder – grated from rod (Alfa Aesar, 99.9%), Mg powder (Alfa Aesar, -325 mesh, 99.8%), and Ni powder (Aldrich, 5 μm , 99.99%) were used. $\text{La}_{2-x}\text{Mg}_x\text{Ni}_7$ ($x = 0.00, 0.25, 0.50,$ and 0.75) alloys powders were prepared by the MA and annealing process. The MA was performed using the SPEX 8000 Mixer Mill. A protective argon atmosphere was applied. Elemental powders (La, Mg, Ni) were weighted, blended and poured into vials in glove box (Labmaster 130) filled with controlled argon atmosphere ($\text{O}_2 < 2$ ppm and $\text{H}_2\text{O} < 1$ ppm). A composition of starting materials mixture was based on a stoichiometry of an *ideal* reaction. However, due to oxidation of La and Mg the content of theses element was increased by 8 wt%. The amount of La and Mg extra addition (8 wt%) was determined during our basic research (not shown here), in order to obtain after MA process and annealing, materials with chemical composition as close as it is possible to stoichiometry of an *ideal* reaction. In all cases the MA process lasted for 48 h in argon atmosphere. In all cases the as-milled materials were heat treated in high purity argon atmosphere at 1123 K for 0.5 h. Furthermore for the reference reasons in XPS characterization the standard La, Mg, and Ni thin films with thicknesses of about 200 nm were prepared at room temperature using computer-controlled UHV magnetron co-sputtering [14]. Ni and Mg (La) targets were sputtered using DC and RF modes, respectively. The base pressure before the deposition process was lower than 5×10^{-10} mbar. As a substrate we used Si(100)

wafers with an oxidized surface to prevent a silicide formation. Therefore we applied a special heat treatment in ultra high vacuum (UHV) before deposition in order to obtain an epitaxial SiO_2 surface layer [15, 16]. The distance between sputtering targets and substrate was about 220 mm. Typical sputtering conditions are listed in Tab. 1. The chemical composition and the cleanness of all layers was checked *in situ* immediately after deposition. The samples were transferred to an UHV (4×10^{-11} mbar) analysis chamber equipped with XPS, Auger electron spectroscopy (AES) and ion gun etching system.

Table 1: Typical sputtering conditions used for the deposition of La, Mg and Ni thin films.

Parameter	Unit	La, Mg	Ni
Rest gas pressure	mbar	5×10^{-10}	
Argon partial pressure	mbar	1×10^{-3}	
Argon purity	%	99.9998	
Target diameter	mm	51	
Target purity	%	99.95	99.95
Distance between substrate and target	mm	220	
Sputtering method	-	Magnetron RF	Magnetron DC
Sputtering power	W	40-60	30-50
Deposition rate	nm/s	0.01-0.07	0.01-0.1
Substrate temperature during deposition	K	295	

2.2. Structural Characterization

The crystallographic structures of the $\text{La}_{2-x}\text{Mg}_x\text{Ni}_7$ samples were investigated at room temperature using the Panalytical Empyrean XRD with $\text{Cu K}\alpha_1$ ($\lambda = 1.54056 \text{ \AA}$) radiation. The conditions of XRD measurements were: voltage 45 kV, anode current 40 mA and 2 Theta range 20° – 80° .

2.3. Electrochemical Measurements

Mechanically alloyed and annealed materials, in nanocrystalline form, with 10 wt.% addition of Ni powder, were used to form metal-hydride electrodes. Materials were pressed (1050 MPa) with nickel nets acting as current collector to 0.5 g pellets. The diameter of each electrode was 8.0 mm and the weight was approximately 0.3 g. Initial activation was carried out by soaking of the electrode in 6 M KOH for 24 h at room temperature. Electrochemical measurements were made using the Multi-channel Battery Interface ATLAS 0461 and ATLAS 0961. Studies were done in an open three-compartment glass cell, using a much larger $\text{NiOOH}/\text{Ni}(\text{OH})_2$ counter electrode and a mercury oxide ($\text{Hg}/\text{HgO}/6 \text{ M KOH}$) reference

electrode. The electrodes were charged and discharged at 40 mA/g and the cut-off potential *vs* Hg/HgO/6 M KOH amounts to -0.7 V. All electrochemical measurements were carried out in deaerated 6 M KOH solution prepared from pure KOH and 18 MΩ/cm water, at temperature of about 293 K. Cycle stability (R_h) of materials was evaluated by capacity retaining rate after n cycle: $R_h = (C_n/C_{max}) \times 100\%$, where C_n and C_{max} are discharge capacities at the n -th cycle and maximum discharge capacity, respectively.

2.4. XPS Measurements

The XPS spectra were measured at room temperature using the SPECS EA 10 PLUS energy spectrometer with Al- K_{α} radiation of 1486.6 eV. For the XPS valence band measurements we used a step size equal to 0.05 eV. The energy spectra of the electrons were analyzed by a hemispherical analyzer (FWHM_{Mg-K α} equals 0.8 eV for Ag 3d_{5/2}). Calibration of the spectra was performed according to Baer *et al.* [17]. The emission spectra of La, Mg and Ni were measured immediately after the sample transfer from the preparation chamber in a vacuum of 8×10^{-11} mbar. The 4f_{7/2} peak of gold was situated at 84.0 eV and the Fermi level was located at binding energy 0 eV. The surface layer with impurities (~ 10 nm) of the studied bulk nanocrystalline samples could be removed using a SPECS ion gun etching system. We have used 3 keV Ar⁺ ion beam that was incident at an angle of 45° to the surface of the sample [18]. The measurements were conducted following routine backing procedures ($T = 440$ K) of the analysis chamber which made possible reaching a base vacuum of 4×10^{-11} mbar. Details of the XPS measurements can be found in Refs. [14, 19, 20].

2.5. Density Functional Theory Calculations

The electronic band structure calculations of several phases related to (La,Mg)₂Ni₇ samples were carried out using the full-potential local-orbital minimum-basis scheme [21, 22]. The utilized FPLO5.00 version of the code is the latest public version allowing for the calculations within coherent potential approximation (CPA) [23]. The CPA was used to computationally model a chemical disorder as introduced to crystal structures of La₂Ni₇ by substituting Mg on La sites. The form of CPA implementation in the FPLO5 prevents us from applying full-relativistic scheme and allows to use only a scalar-relativistic one. Nevertheless, the constituent light elements (La, Mg, Ni) and the scope of this study justify the application of this approach. Moreover, the additional full relativistic calculations made by us confirm this assumption. For all calculations we use the local density approximation (PW92) [24], optimization of the basis, 16³ k-mesh and convergence criterion of charge density 10⁻⁶. One exception is the La_{1.5}Mg_{0.5}Ni₇ in Ce₂Ni₇-type structure for which we had to limit the k-mesh down to 6³. Although the hexagonal La₂Ni₇ undergoes an antiferromagnetic transition at $T_N = 51$ K [25], we consider only

non-magnetic models as consistent with the non-magnetic states of the samples in room temperature. The theoretical photoemission spectra were obtained from the calculated densities of electronic states convoluted by Gaussian with a half-width (δ) equal to 0.6 eV and scaled using the proper photoelectronic cross-sections for partial states [26]. This method we have successfully used before to calculate photoemission spectra of CeRh₃Si₂ and UGe₂ [27, 28]. The intention for convolution by Gaussian is to mimic a lifetime of hole states, an experimental broadening from instrumental resolution and thermal effects. The value of $\delta = 0.6$ eV is selected as close to the value identified for the spectrometer used for measurements.

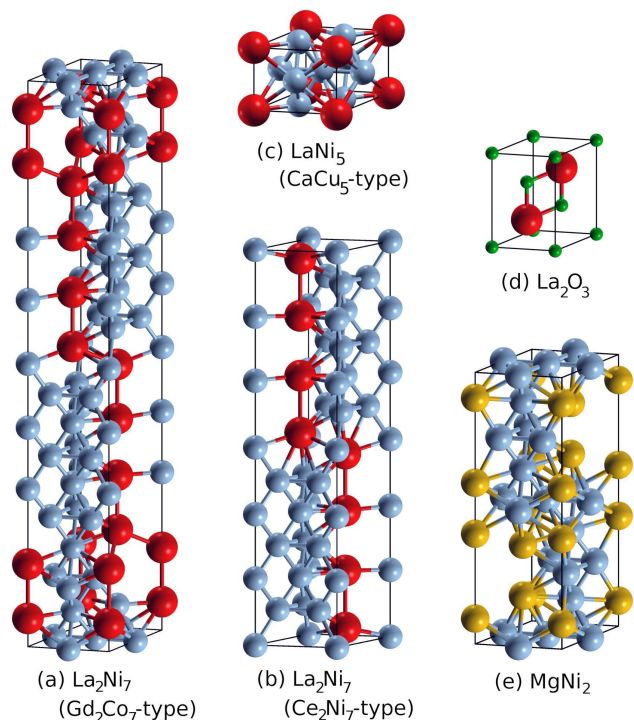


Figure 1: The crystal structures of several compounds related to the considered (La,Mg)₂Ni₇ samples. (a) La₂Ni₇ in Gd₂Co₇-type structure; (b) La₂Ni₇ in Ce₂Ni₇-type structure; (c) LaNi₅ in CaCu₅-type structure; (d) La₂O₃; (e) MgNi₂ (C36). The different atoms are denoted by different colors as follows: La – red, Ni – blue, O – green, Mg – yellow.

From first principles we calculate electronic structures of several phases identified by XRD in the considered (La,Mg)₂Ni₇ samples. They are Ce₂Ni₇-type and Gd₂Co₇-type phases of La₂Ni₇, LaNi₅ and La₂O₃. Furthermore we calculate *ab initio* the bcc Ni and MgNi₂ (C36) phases. Except for La₂Ni₇ with Gd₂Co₇-type structure, we use the lattice parameters and atomic coordinates as refined in experiments [29, 30, 31, 32, 33]. In the face of lack in literature of the refined atomic positions for Gd₂Co₇-type structure of La₂Ni₇, we have optimized for this phase the initial atomic coordinates of isostructural Y₂Ni₇ (Gd₂Co₇-type) [29]. The optimized atomic positions with hexagonal and rhombohedral axes are col-

Table 2: The basic structural data of five compounds related to the considered (La,Mg)₂Ni₇ samples as used for *ab initio* calculations.

phase	prototype	space group	no.	<i>a</i> (Å)	<i>c</i> (Å)	Ref.
La ₂ Ni ₇	Ce ₂ Ni ₇	<i>P6₃/mmc</i>	194	5.07	24.56	this work
La ₂ Ni ₇	Gd ₂ Co ₇	<i>R$\bar{3}m$</i>	166	5.056	36.98	[29]
LaNi ₅	CaCu ₅	<i>P6/mmm</i>	191	5.010	3.972	[30]
MgNi ₂	MgNi ₂	<i>P6₃/mmc</i>	194	4.8256	15.8323	[31]
La ₂ O ₃	La ₂ O ₃	<i>P$\bar{3}m1$</i>	164	3.9381	6.1361	[32]

Table 3: Crystallographic parameters of La₂Ni₇ in Ce₂Ni₇-type structure reproduced after Levin *et al.* [33]. Lattice parameters *a* = 5.0577, *c* = 24.7336 Å, space group *P6₃/mmc*.

atom	site	<i>x</i>	<i>y</i>	<i>z</i>
La ₁	4 <i>f</i>	1/3	2/3	0.03013
La ₂	4 <i>f</i>	1/3	2/3	0.17422
Ni ₁	2 <i>a</i>	0	0	0
Ni ₂	4 <i>e</i>	0	0	0.16898
Ni ₃	4 <i>f</i>	1/3	2/3	0.83616
Ni ₄	6 <i>h</i>	0.8341	0.6682	1/4
Ni ₅	12 <i>k</i>	0.8350	0.6700	0.08806

Table 4: Crystallographic parameters of La₂Ni₇ in Gd₂Co₇-type structure – space group *R $\bar{3}m$* (no. 166) hexagonal axes ($\alpha = \beta = 90^\circ, \gamma = 120^\circ$). Lattice parameters *a* = 5.056, *c* = 36.98 Å as measured by Virkar and Raman [29]. Atomic positions relaxed with use of the FPLO DFT code.

atom	site	<i>x</i>	<i>y</i>	<i>z</i>
La ₁	6 <i>c</i>	0	0	0.0501
La ₂	6 <i>c</i>	0	0	0.1459
Ni ₁	3 <i>b</i>	0	0	1/2
Ni ₂	6 <i>c</i>	0	0	0.2790
Ni ₃	6 <i>c</i>	0	0	0.3871
Ni ₄	9 <i>e</i>	1/2	0	0
Ni ₅	18 <i>h</i>	1/2	-1/2	0.1077

Table 5: Crystallographic parameters of La₂Ni₇ in Gd₂Co₇-type structure – space group *R $\bar{3}m$* (no. 166) rhombohedral axes. Lattice parameters *a* = *b* = *c* = 12.6676 Å and $\alpha = \beta = \gamma = 23.02^\circ$ converted to rhombohedral representation from crystal refinements made by Virkar and Raman [29]. Atomic positions relaxed with use of the FPLO DFT code.

atom	site	<i>x</i>	<i>y</i>	<i>z</i>
La ₁	6 <i>c</i>	0.0501	0.0501	0.0501
La ₂	6 <i>c</i>	0.1459	0.1459	0.1459
Ni ₁	3 <i>b</i>	-1/2	-1/2	-1/2
Ni ₂	6 <i>c</i>	0.2790	0.2790	0.2790
Ni ₃	6 <i>c</i>	0.3871	0.3871	0.3871
Ni ₄	9 <i>e</i>	-1/2	1/2	0
Ni ₅	18 <i>h</i>	-0.3931	0.1092	-0.3931

lected in Tables 4 and 5. They are in good agreement with the atomic positions refined with Rietveld analysis

for isostructural La_{1.5}Mg_{0.5}Ni₇ (Gd₂Co₇-type) [34]. Furthermore, Tab. 3 presents the crystallographic parameters of La₂Ni₇ in Ce₂Ni₇-type structure as measured by Levin *et al.* [33] and used by us for calculations. The collection of basic structural data for other phases taken into account is presented in Tab. 2. The considered crystal structures are also shown in Fig. 1. For La_{1.5}Mg_{0.5}Ni₇ systems modeled in CPA we used the experimental lattice parameters. As the FPLO code precludes optimization if the CPA applied, the atomic positions were used as for corresponding La₂Ni₇ structures. For visualization of crystal structures the XCrySDen computer code [35] was used.

3. Results and Discussion

The La_{2-x}Mg_xNi₇ alloys powders (*x* = 0.00, 0.25, 0.50 and 0.75) were prepared by the MA and annealing process. In this section we will present the results and discussion of structural and valence band characterization, electrochemical measurements and *ab initio* calculations.

3.1. Structural Characterization

Table 6: XRD resolved lattice parameters of Ce₂Ni₇-type phase and electrochemical properties of La_{2-x}Mg_xNi₇ alloys. Maximum discharge capacities (*C_{max}*), discharge capacities at 30 cycles (*C₃₀*) and cycle stability (*R_h*).

<i>x</i>	<i>a</i> Å	<i>c</i> Å	<i>V</i> Å ³	<i>C_{max}</i> mAh/g	<i>C₃₀</i> mAh/g	<i>R_h</i>
0.00	5.07	24.56	546.58	76	30	39
0.25	5.06	24.49	543.56	213	146	69
0.50	5.04	24.20	533.21	304	204	67
0.75	5.03	24.22	531.26	237	226	95

After 48 h of MA the originally sharp diffraction peaks (not shown) of the constituent elements La, Mg and Ni lost their intensity. The subsequent heat treatment at 1123 K for 0.5 h (under high purity argon atmosphere) induces crystallization in the La_{2-x}Mg_xNi₇ samples. Accordingly to XRD patterns, in the final La_{2-x}Mg_xNi₇ samples no single-element phases of La, Mg nor Ni was present. The XRD spectra of the resultant La_{2-x}Mg_xNi₇ alloys are presented in Fig. 2. Table 6 presents how the lattice parameters of Ce₂Ni₇-type phase decrease with Mg concentration. Based on the peaks intensities analysis we conclude that

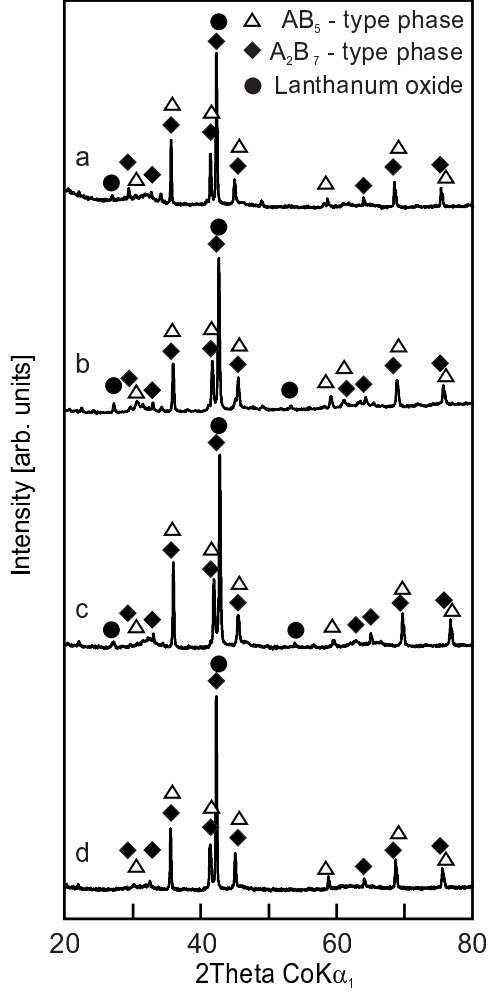


Figure 2: The XRD spectra of $\text{La}_{2-x}\text{Mg}_x\text{Ni}_7$ after 48 h mechanical alloying and annealing at 1123 K for 0.5 h. (a) $x = 0.00$, (b) $x = 0.25$, (c) $x = 0.50$ and (d) $x = 0.75$.

Table 7: The composition of La_2Ni_7 and $\text{La}_{1.5}\text{Mg}_{0.5}\text{Ni}_7$ samples (in wt.% of the constituent phases).

phase	La_2Ni_7	$\text{La}_{1.5}\text{Mg}_{0.5}\text{Ni}_7$
La_2Ni_7 (Ce_2Ni_7 -type)	46.1	16.0
La_2Ni_7 (Gd_2Co_7 -type)	46.1	72.9
LaNi_5	5.6	8.0
La_2O_3	2.2	3.1

the resultant La_2Ni_7 sample has the multi-phase character and consists of Ce_2Ni_7 -type (46.1 wt.%) and Gd_2Co_7 -type (46.1 wt.%) structures of La_2Ni_7 phase, LaNi_5 (5.6 wt.%) and La_2O_3 (2.2 wt.%) phases. In the $\text{La}_{1.5}\text{Mg}_{0.5}\text{Ni}_7$ sample ($x = 0.5$) the Gd_2Co_7 -type of La_2Ni_7 phase (72.9 wt.%) prevails with a smaller share of Ce_2Ni_7 -type (16.0 wt.%) of La_2Ni_7 and additions of LaNi_5 (8.0 wt.%) and La_2O_3 (3.1 wt.%). For $\text{La}_{1.5}\text{Mg}_{0.5}\text{Ni}_7$ sample Zhang *et al.* reported composition of about 60% Gd_2Co_7 -type and 40% Ce_2Ni_7 -type phase after annealing at above 1000 K, which

stays in relatively good agreement with our result. [34] The data on phase composition of La_2Ni_7 and $\text{La}_{1.5}\text{Mg}_{0.5}\text{Ni}_7$ samples are gathered in Tab. 7. The collection of basic structural parameters of the $\text{La}_{2-x}\text{Mg}_x\text{Ni}_7$ constituent phases can be found in Tab. 2 and Fig. 1 gives their graphical representations. The Ce_2Ni_7 -type and Gd_2Co_7 -type structures of La_2Ni_7 phase are closely related. They crystallize in $P6_3/mmc$ and $R\bar{3}m$ space groups, respectively. The crystal structures are highly anisotropic and can be understood as stacking of LaNi_5 and LaNi_2 unit blocks along the c axis [12]. An almost equal concentration of the Ce_2Ni_7 -type and Gd_2Co_7 -type structures in our La_2Ni_7 sample can be understood based on by nearly identical heat of formation of these structures [12]. The heat of formation analysis indicates also that in the case of $\text{La}_{1.5}\text{Mg}_{0.5}\text{Ni}_7$ sample a preferred atomic positions of Mg/La substitutions are $4f_1$ in case of Ce_2Ni_7 -type and $6c_2$ in Gd_2Co_7 -type structure [12]. The complete tables with atomic coordinates of La_2Ni_7 phases can be found in Sec. 2.5. The detailed crystallographic structures of metal hydrides $\text{La}_2\text{Ni}_7\text{D}_x$ [36] and $\text{La}_{1.5}\text{Mg}_{0.5}\text{Ni}_7\text{D}_x$ [37] (of Ce_2Ni_7 -type structure) have been refined.

3.2. Electrochemical Measurements

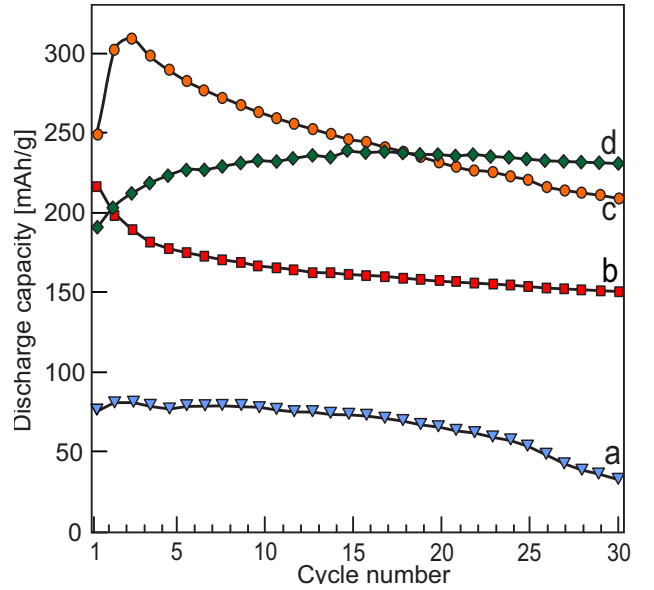


Figure 3: Discharge capacities as a function of cycle number of $\text{La}_{2-x}\text{Mg}_x\text{Ni}_7$. (a) $x = 0.00$, (b) $x = 0.25$, (c) $x = 0.50$ and (d) $x = 0.75$.

Results of electrochemical measurements for $\text{La}_{2-x}\text{Mg}_x\text{Ni}_7$ alloys ($x = 0.00, 0.25, 0.50$ and 0.75) are presented in Fig. 3 as discharge capacities in function of cycle number. Furthermore, the measured electrochemical characteristics of the materials are summarized in Tab. 6. It is concluded that the best activation properties has the unmodified La_2Ni_7 alloy and an addition of Mg causes only deterioration of the activation

properties. The activation capability of an alloy electrode is related to the change of the internal energy of the hydride system before and after hydrogen absorption [5]. The electrochemical properties of the alloy depends on multiple factors, involving its crystal structure, phase composition and microstructure. Most of the electrodes display maximum discharge capacity (C_{max}) during the first three cycles. C_{max} is increasing with Mg content to reach the highest value (304 mAh/g) for $x = 0.5$ ($\text{La}_{1.5}\text{Mg}_{0.5}\text{Ni}_7$). Further increase of Mg concentration causes decrease of C_{max} . The same tendency was observed in pressure-composition-temperature (PCT) tests [11]. The degradation of discharge capacity in La-Mg-Ni alloys originates from forming and increasing of $\text{Mg}(\text{OH})_2$ and $\text{La}(\text{OH})_3$ surface layers. These oxides hinder the hydrogen atoms from diffusion in or out in alkaline solutions [38]. Partial substitution of La by Mg

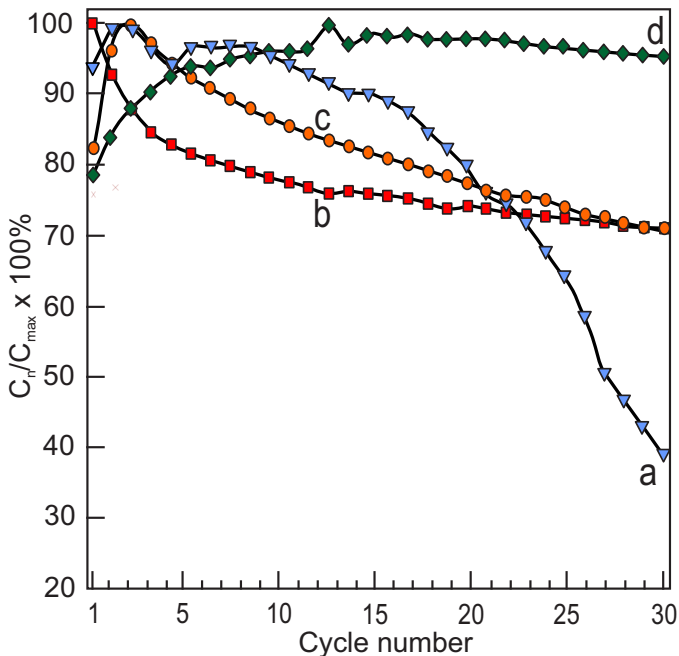


Figure 4: Cyclic stability of electrodes prepared from $\text{La}_{2-x}\text{Mg}_x\text{Ni}_7$ alloys. (a) $x = 0.00$, (b) $x = 0.25$, (c) $x = 0.50$ and (d) $x = 0.75$.

causes increase of cycle stability of electrodes, see Fig. 4. The best cycle stability was obtained for the material where $x = 0.75$. It is due to the phase composition of this material. In $\text{La}_{1.25}\text{Mg}_{0.75}\text{Ni}_7$ alloy, except the main $(\text{La},\text{Mg})_2\text{Ni}_7$ phase, the LaNi_5 phase is observed, which possesses much higher electrochemical cycle stability than $(\text{La},\text{Mg})_2\text{Ni}_7$ phase [39]. Taking into account the C_{max} , a sample with the most promising composition is $\text{La}_{1.5}\text{Mg}_{0.5}\text{Ni}_7$ ($x = 0.5$) and further investigations presented in this work will focus on it.

3.3. XPS Measurements

It has been shown that the formation of metal hydrides follows the rules of semi-empirical models [40, 41], which characteristic parameters depend on the features of the

valence band. One of the experimental technique of characterization of the valence band is the X-ray photoelectron spectroscopy (XPS). The analysis of the valence band provides information on electronic structure together with features of crystal structure and microstructure. These electronic and geometric factors affect the metal-hydrogen interaction. The measured XPS valence band spectra are

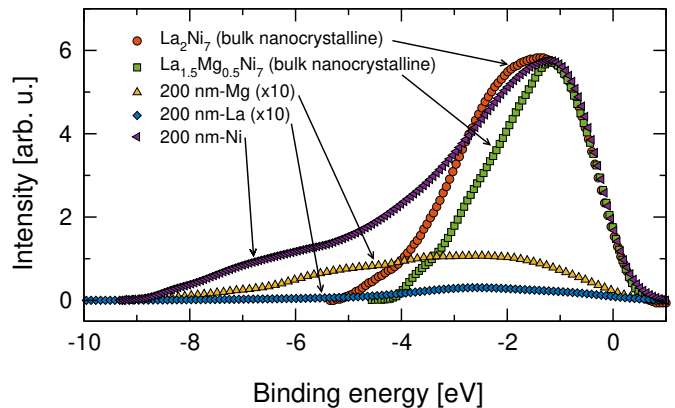


Figure 5: The XPS valence band spectra (Al-K_{α}) of bulk nanocrystalline La_2Ni_7 and $\text{La}_{1.5}\text{Mg}_{0.5}\text{Ni}_7$ alloys, together with valence band spectra of *in situ* prepared pure La, Mg and Ni thin films presented for comparison.

presented in Fig. 5. Instead of investigating the whole range of $\text{La}_{2-x}\text{Mg}_x\text{Ni}_7$ compositions with the XPS, we focus on the $\text{La}_{1.5}\text{Mg}_{0.5}\text{Ni}_7$ sample which, among the investigated series, exhibited the highest value of discharge capacity ($C_{max} = 304$ mAh/g). As reference we study with XPS also the bulk nanocrystalline La_2Ni_7 sample and *in situ* prepared La, Mg and Ni thin films. The XPS spectra of the elemental thin films suggest that the main contribution to the La_2Ni_7 and $\text{La}_{1.5}\text{Mg}_{0.5}\text{Ni}_7$ valence bands comes from the $3d$ electrons of Ni. The full width at half maximum (FWHM) of the La_2Ni_7 and $\text{La}_{1.5}\text{Mg}_{0.5}\text{Ni}_7$ valence bands are about 2.7 eV and 2.2 eV, respectively. The narrowing of the $\text{La}_{1.5}\text{Mg}_{0.5}\text{Ni}_7$ valence band could be explained by increase of amount of the La oxide phase in the surface layer. This concept will be investigated in the next section covering the *ab initio* results. Note, that the XPS signal originates mainly from the surface layer (3–5 nm) [18, 42]. Furthermore, in Ref. [18] we showed that La atoms segregate to the surface of the nanocrystalline LaNi_5 -type alloys and form stable oxides under ambient conditions. The oxidized top layer is depth-limited and forms a good protective layer against further oxidation under ambient conditions. As described in Sec. 2.4, we have removed only of about 10 nm surface impurity layer which mainly consisted of carbon and oxygen. However, the subsurface layer composed of a significant amount of La oxides was not removed. In the case of nanocrystalline La_2Ni_7 alloy the content of the oxide in the subsurface layer is significantly lower probably due to negligible La segregation effect. The above result is in good agreement with average La_2O_3 content estimated from the XRD experiment,

see Tab. 7. Therefore, the valence band of the nanocrystalline $\text{La}_{1.5}\text{Mg}_{0.5}\text{Ni}_7$ is narrower compared to that measured for the La_2Ni_7 alloy. Theoretical XPS valence bands calculated for perfect crystalline materials without segregation and oxidation effects are practically the same, see Sec. 3.4.2. Furthermore, looking from other perspective, such an additional surface oxide layer could influence hydrogen absorption and electrochemical properties of the studied material, as has been recently reported for the well defined Mg/Pd bilayers with La interlayer [43].

3.4. Density Functional Theory Calculations

In DFT calculations, similar like in the XPS measurements, we focus on the $\text{La}_{1.5}\text{Mg}_{0.5}\text{Ni}_7$ sample with the highest C_{max} instead of considering the whole concentration range of Mg. It has been shown that the inhomogeneous $\text{La}_{1.5}\text{Mg}_{0.5}\text{Ni}_7$ sample consists, among others, of $\text{La}_{1.5}\text{Mg}_{0.5}\text{Ni}_7$ in Ce_2Ni_7 -type and Gd_2Co_7 -type phases, LaNi_5 and La_2O_3 , see Tab. 7. Furthermore, for the neighboring composition (LaMgNi_7) Crivello *et al.* [12] suggested an energetically stable state with LaNi_5 phase coexisting with MgNi_2 . The above observations are the reason why we decide to investigate theoretically the several phases mentioned above. That list has been extended by the reference phases: Ce_2Ni_7 -type and Gd_2Co_7 -type of La_2Ni_7 and fcc Ni. This analysis is designed to answer the questions of the energetic stability of the particular phases and to better understand the electronic properties and the nature of $\text{La}_{1.5}\text{Mg}_{0.5}\text{Ni}_7$ valence band (studied in this work also by XPS). The basic structural data of the considered phases are collected in Tabs. 2, 3, 4 and 5. For graphical representation of crystallographic structures see Fig. 1.

3.4.1. Site preference and phase stability

Our calculations on LaNi_5 , La_2O_3 , MgNi_2 and fcc Ni are dedicated to resolve the measured XPS valence band of inhomogeneous samples. However nearly 90% of the $\text{La}_{1.5}\text{Mg}_{0.5}\text{Ni}_7$ composition consists of Ce_2Ni_7 -type and Gd_2Co_7 -type phases, see Tab. 7. This is why the latter phases are the main subject of our DFT study. Although the basic La_2Ni_7 phases can be simulated based on the simple ordered structures, the modeling of the systems with chemical disorder is more demanding. Previously the $\text{La}_{2-x}\text{Mg}_x\text{Ni}_7$ systems with Mg have been modeled based on the ordered compound method [6, 12]. In this work the chemical disorder introduced by Mg substitution on La sites is considered based on the coherent potential approximation (CPA). One of the advantages of CPA method is that it allows for any arbitrary concentration and not only $x = 0.5, 1.0$ or 1.5 . We have applied the CPA before to model Nb and Ti substitutions in YCo_2 [44].

Experimental observations of phase composition indicate about 46 wt.% shares of hexagonal Ce_2Ni_7 -type and rhombohedral Gd_2Co_7 -type phases in our La_2Ni_7 samples, see Tab. 7. The formation of significant amounts of both

phases suggests small energy difference between them, which finds a confirmation in nearly identical heats of formation calculated by Crivello *et al.* [12] for La_2Ni_7 in two above structure types. So good energy balance between both types of structures comes from a close relationship between them, consisting both of LaNi_2 and LaNi_5 unit blocks [12]. The total energy comparison made by us indicates that both structure types have nearly the same total energies with a small preference of about 10 meV/atom in favor of Gd_2Co_7 -type which is in good agreement with the previous results [12]. Furthermore, the total energy comparison between hexagonal and rhombohedral phases of $\text{La}_5\text{Ni}_{19}$ [7] indicates a very small preference of about 1.4 meV/atom in favor of hexagonal phase. The above results of small energy differences together with the heats of formation calculated by Crivello *et al.* [12] suggest that in the whole La-Ni-Mg system might be difficult to find preference of hexagonal or rhombohedral-type structures.

In $\text{La}_{1.5}\text{Mg}_{0.5}\text{Ni}_7$ samples with 25% doping of Mg on La sites also occur hexagonal Ce_2Ni_7 -type and rhombohedral Gd_2Co_7 -type phases. In order to describe site preferences for Mg, both structure types have to be considered. Zhang *et al.* [45] determined from Rietveld analysis that the Mg atoms are located only on the $4f$ La₁ sites (in Laves unit blocks LaNi_2) of hexagonal $\text{La}_{1.5}\text{Mg}_{0.5}\text{Ni}_7$ phase (Ce_2Ni_7 -type), see Tab. 3. The same conclusions were drawn once again by Denys *et al.* [37]. The beneficial conditions for Mg substitution on La $4f_1$ site ($\Delta E \sim 60$ meV/atom) were also predicted with DFT [12]. We have once again attempted to determine the Mg site preferences in $\text{La}_{1.5}\text{Mg}_{0.5}\text{Ni}_7$ (Ce_2Ni_7 -type), but this time based on the CPA models. We consider Mg atoms located at $4f_1$ sites, $4f_2$ sites or randomly distributed between them. Our total energy calculations show that the most stable configuration is when the Mg atoms are located at La $4f_1$ sites, and the least probable is random distribution of dopants between $4f_1$ and $4f_2$ sites. The difference in total energy between these configurations is about 70 meV/atom, which is relatively large value and suggests rather strong preference, even above room temperature.

For Gd_2Co_7 -type phase of $\text{La}_{1.5}\text{Mg}_{0.5}\text{Ni}_7$ Zhang *et al.* [34] determined experimentally that Mg atoms prefer to occupy the La₂ $6c_2$ sites, however together with minor tendency towards the La₁ $6c_1$ sites, see Tabs. 4 and 5. Based on the DFT calculations Crivello *et al.* [12] also indicated for Gd_2Co_7 -type phase of $\text{La}_{1.5}\text{Mg}_{0.5}\text{Ni}_7$ the $6c_2$ sites preference of Mg ($\Delta E \sim 60$ meV/atom).

In case of $\text{La}_{1.5}\text{Mg}_{0.5}\text{Ni}_7$ sample our diffraction refinement indicates 16% of Ce_2Ni_7 -type and 72.9% of Gd_2Co_7 -type phase, see Tab. 7. Previously Zhang *et al.* reported also the composition of about 60% Gd_2Co_7 -type and 40% Ce_2Ni_7 -type phase in $\text{La}_{1.5}\text{Mg}_{0.5}\text{Ni}_7$ sample [34]. Similar like for La_2Ni_7 samples, the formation of both phases suggests small energy difference between them. Based on DFT calculations Crivello *et al.* [12] found nearly identical heats of formation for both hexagonal and rhombohedral ground state structures of $\text{La}_{1.5}\text{Mg}_{0.5}\text{Ni}_7$. Our total energy cal-

culations comparing $\text{La}_{1.5}\text{Mg}_{0.5}\text{Ni}_7$ phase of Ce_2Ni_7 -type and Mg at $4f_1$ sites with $\text{La}_{1.5}\text{Mg}_{0.5}\text{Ni}_7$ of Gd_2Co_7 -type phase and Mg at $6c_2$ sites gives energy difference of about 100 meV/atom with a preference of Gd_2Co_7 -type phase.

Concluding, the La_2Ni_7 and $\text{La}_{1.5}\text{Mg}_{0.5}\text{Ni}_7$ phases are stable in both hexagonal Ce_2Ni_7 -type and rhombohedral Gd_2Co_7 -type structures. In $\text{La}_{1.5}\text{Mg}_{0.5}\text{Ni}_7$ phase the Mg site preferences are $4f_1$ in hexagonal and $6c_2$ in rhombohedral structure types. These two ground state $\text{La}_{1.5}\text{Mg}_{0.5}\text{Ni}_7$ structures, together with two La_2Ni_7 structures will be considered in the next section devoted to the analysis of the valence band.

3.4.2. Valence band analysis

Our valence band DFT calculations are dedicated both as (1) interpretation for experimental XPS and (2) self-standing results shedding light on the electronic structure of the $\text{La}_{1.5}\text{Mg}_{0.5}\text{Ni}_7$ and at the same time filling the gap in understanding of the system. The valence bands of both La_2Ni_7 and $\text{La}_{1.5}\text{Mg}_{0.5}\text{Ni}_7$ phases in hexagonal Ce_2Ni_7 -type and rhombohedral Gd_2Co_7 -type structures are presented in Fig. 6. There is not much differences between the densities of states (DOS) calculated for hexagonal and rhombohedral phases. The main part of the valence bands start in each case about -5.0 eV and finish soon after Fermi energy (E_F). In every case two main maxima (at -2.3 and -0.8 eV) and characteristic sharp peak around E_F are observed. The main contributions to the valence bands come from the Ni 3d bands, see Fig. 7(a), and resemble the valence band of the bcc Ni, see Fig. 7(d).

As Mg atoms have one less valence electron than La ones the substitution of Mg in place of La in La_2Ni_7 slightly depopulates the valence band. In terms of rigid band approximation the Fermi level (E_F) of $\text{La}_{1.5}\text{Mg}_{0.5}\text{Ni}_7$ shifts a little bit left towards the higher binding energies, see Figs. 7(b) and (c). It is observed that the Ni atoms in $\text{La}_{1.5}\text{Mg}_{0.5}\text{Ni}_7$ have about 0.4 less of 3d electrons per band than in La_2Ni_7 . In case of La_2Ni_7 even a small change in valence band occupation may significantly affect the conduction properties of the material, as the sharp peak is located at the Fermi level. In fact, the Mg substitution in $\text{La}_{1.5}\text{Mg}_{0.5}\text{Ni}_7$ reduces the value of $\text{DOS}(E_F)$ from about 30 to 11 states/(eV f.u.) for hexagonal Ce_2Ni_7 -type structure and from about 29 to 14 states/(eV f.u.) for the rhombohedral Gd_2Co_7 -type structure. These values of $\text{DOS}(E_F)$ correspond to the parameter γ in linear term of specific heat of 72 and 25 mJ/(molK²) for hexagonal and 68 and 34 mJ/(molK²) for rhombohedral structure, respectively. The above values of $\text{DOS}(E_F)$ and γ consist mainly of contributions from Ni electrons (above 95%).

In Fig. 5 we present the measured XPS valence band spectra of bulk nanocrystalline La_2Ni_7 and $\text{La}_{1.5}\text{Mg}_{0.5}\text{Ni}_7$ alloys. As the XPS resolution is limited the observed spectra are rather fuzzy. The FWHM of the La_2Ni_7 and $\text{La}_{1.5}\text{Mg}_{0.5}\text{Ni}_7$ valence bands are about 2.7 eV and 2.2 eV, respectively. In Fig. 7(e) and (f) we show the calculated XPS spectra of La_2Ni_7 and $\text{La}_{1.5}\text{Mg}_{0.5}\text{Ni}_7$ based on the

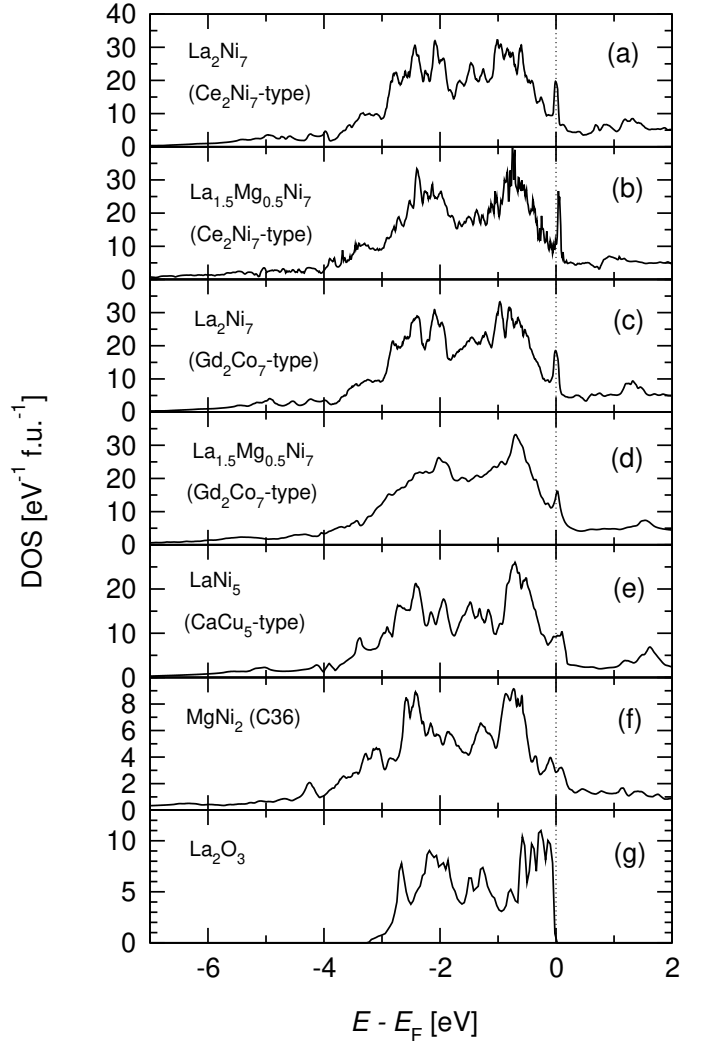


Figure 6: Densities of states (DOS) calculated for (a) $\text{La}_{2-x}\text{Mg}_x\text{Ni}_7$ (Ce_2Ni_7 -type), (b) $\text{La}_{1.5}\text{Mg}_{0.5}\text{Ni}_7$ (Ce_2Ni_7 -type), (c) La_2Ni_7 (Gd_2Co_7 -type), (d) $\text{La}_{1.5}\text{Mg}_{0.5}\text{Ni}_7$ (Gd_2Co_7 -type), (e) LaNi_5 , (f) MgNi_2 (C36) and (g) La_2O_3 phases.

DOS of hexagonal Ce_2Ni_7 -type structures. The calculated valence band width FWHM of La_2Ni_7 of about 2.8 eV stays in very good agreement with the measurements. As the addition of Mg shifts the DOS only slightly, the resultant theoretical XPS spectra of $\text{La}_{1.5}\text{Mg}_{0.5}\text{Ni}_7$ are then also nearly identical as for La_2Ni_7 and its FWHM is about 2.7 eV. This number is much bigger than experimental 2.2 eV for $\text{La}_{1.5}\text{Mg}_{0.5}\text{Ni}_7$ sample and from theory we can conclude that the narrowing of experimental XPS of $\text{La}_{1.5}\text{Mg}_{0.5}\text{Ni}_7$ in respect to La_2Ni_7 cannot be explained based on the single phase arguments. Trying to find the origins for such narrowing we considered from DFT the valence bands of LaNi_5 , La_2O_3 , bcc Ni and MgNi_2 (C36) phases, which all may be part of the $\text{La}_{1.5}\text{Mg}_{0.5}\text{Ni}_7$ sample, see Figs. 6(e-g) and 7(d). The comparison of the calculated DOS's indicates that all considered structures with Ni have very similar width of the valence band. Therefore the experi-

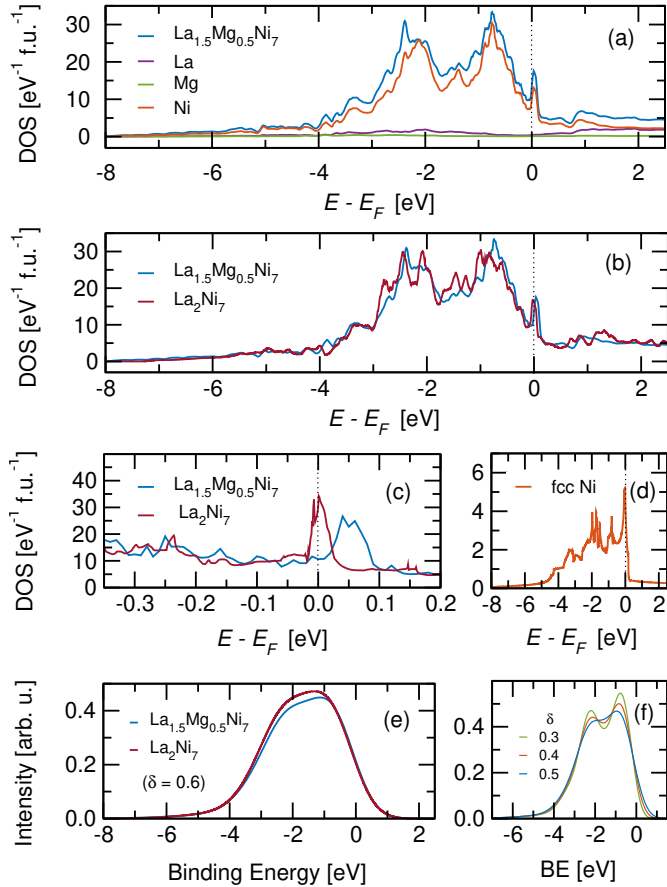


Figure 7: (a) Density of states (DOS) for $\text{La}_{1.5}\text{Mg}_{0.5}\text{Ni}_7$ (hexagonal Ce_2Ni_7 -type) together with element-resolved contributions, (b),(c) DOS for La_2Ni_7 and $\text{La}_{1.5}\text{Mg}_{0.5}\text{Ni}_7$ (both Ce_2Ni_7 -type), (d) DOS for fcc Ni, (e) calculated XPS spectra of La_2Ni_7 and $\text{La}_{1.5}\text{Mg}_{0.5}\text{Ni}_7$ (both Ce_2Ni_7 -type), (f) calculated XPS spectra of $\text{La}_{1.5}\text{Mg}_{0.5}\text{Ni}_7$ Ce_2Ni_7 -type for different δ parameters.

mentally observed narrowing of the $\text{La}_{1.5}\text{Mg}_{0.5}\text{Ni}_7$ valence band (FWHM = 2.2 eV) cannot be explained based on the presence of other phases containing Ni. However, the effect of narrowing can be related to the presence of the oxide phase La_2O_3 , which valence band showed in Fig. 6(g) is noticeably narrower from the remaining Ni compounds. In fact, the presence of 3.1 wt.% of La_2O_3 phase have been observed in $\text{La}_{1.5}\text{Mg}_{0.5}\text{Ni}_7$ sample. The theoretical XPS spectra presented in Fig. 7(e) were obtained from the partial DOS's convoluted by Gaussians with a half-width δ equal to 0.6 eV. For smaller δ the XPS spectra would reveal more features of valence band, see Fig. 7(f). The broadening parameter δ of our XPS equipment is however only about 0.4–0.5 eV. Therefore, the double-peak structure observed in theoretical XPS for $\delta = 0.3$ eV, see Fig. 7(f), could not be directly observed experimentally, see Fig. 5. The theoretical XPS spectra are also calculated for the perfect *single-crystalline* materials, when the experimental XPS spectra of the real nanocrystalline samples are further obscured due to broadening coming from a complex microstructure of the material. The broaden-

ing of the experimental valence band of the nanocrystalline La_2Ni_7 alloy could be explained by a strong deformation of the nanocrystals in mechanically alloyed and heat treated samples [46]. For such nanocrystalline samples the interior of the nanocrystal is constrained and the distances between atoms located at the grain boundaries expanded. In Ref. [20] we have compared the XPS valence bands of mechanically alloyed bulk nanocrystalline $\text{LaNi}_{4.2}\text{Al}_{0.8}$ and high-purity poly- and nanocrystalline LaNi_4Al thin films. For this case we have also observed the valence band broadening in the thin film and bulk nanocrystalline material in relation to the polycrystalline sample.

4. Summary and Conclusions

We studied the effect of substitution La by Mg on electrochemical and electronic properties in $\text{La}_{2-x}\text{Mg}_x\text{Ni}_7$ phases. The experimental preparation and characterization part was followed by the detailed DFT study. First, the series of $\text{La}_{2-x}\text{Mg}_x\text{Ni}_7$ samples (with $x = 0.00, 0.25, 0.50$ and 0.75) was obtained by mechanical alloying. Next, they were characterized by XRD, XPS and electrochemical measurements. We concluded that the resultant La_2Ni_7 samples have the multi-phase character and consist mainly of Ce_2Ni_7 -type and Gd_2Co_7 -type structures of $(\text{La},\text{Mg})_2\text{Ni}_7$, with minor contributions of LaNi_5 and La_2O_3 phases. Best electrochemical properties (maximum discharge capacity) were identified for $\text{La}_{1.5}\text{Mg}_{0.5}\text{Ni}_7$ sample. This composition was then a subject of the XPS investigations covering the valence band and reference samples of La, Mg, Ni and La_2Ni_7 . The main contribution from Ni electrons to valence band was established. The observed narrowing of the $\text{La}_{1.5}\text{Mg}_{0.5}\text{Ni}_7$ valence band in respect to La_2Ni_7 is supposed to be caused by increase of the lanthanum oxide phase concentration. With DFT calculations we focused also on the $\text{La}_{1.5}\text{Mg}_{0.5}\text{Ni}_7$ sample, although we considered also the other phases identified by XRD in our multi-phase samples. Our *ab initio* analysis was intended to investigate the energetic stability of the $\text{La}_{2-x}\text{Mg}_x\text{Ni}_7$ phases and to provide information on the $\text{La}_{1.5}\text{Mg}_{0.5}\text{Ni}_7$ valence band. In face of lack of experimental data, first we determined the atomic positions for Gd_2Co_7 -type La_2Ni_7 -phase by structure optimization. We identified the Gd_2Co_7 -type phases as only slightly more stable than the Ce_2Ni_7 -type for both La_2Ni_7 and $\text{La}_{1.5}\text{Mg}_{0.5}\text{Ni}_7$ phases. For modeling of the Mg substitution in $\text{La}_{1.5}\text{Mg}_{0.5}\text{Ni}_7$ phases we used the coherent potential approximation. We conclude from calculations that the Mg atoms prefer to occupy La $4f_1$ sites for Ce_2Ni_7 -type $\text{La}_{1.5}\text{Mg}_{0.5}\text{Ni}_7$ phase and the La $6c_2$ positions for Gd_2Co_7 -type phase. These results stay in good agreement with the previous experimental and theoretical statements. The stability analysis was followed by the valence band investigations – primarily dedicated to interpret the experimental XPS spectra. It confirmed that the $\text{La}_{1.5}\text{Mg}_{0.5}\text{Ni}_7$ valence band consist mainly of the contribution from Ni electrons. The Mg substitution in place of La in $\text{La}_{2-x}\text{Mg}_x\text{Ni}_7$ only

slightly depopulates the valence band. However, as the strongly localized states were identified near the Fermi energy level, even small shift of Fermi level may affect the conductivity of the material.

Acknowledgements

Work supported by the National Science Centre Poland under the decision DEC-2014/15/B/ST8/00088. Part of the computations was performed on the resources provided by the Poznań Supercomputing and Networking Center (PSNC).

References

- [1] R. A. Varin, T. Czujko, and Z. S. Wronski, *Nanomaterials for Solid State Hydrogen Storage* (Springer Science & Business Media, 2009).
- [2] X. D. Li, O. Elkedim, M. Nowak, and M. Jurczyk, *International Journal of Hydrogen Energy* **39**, 9735 (2014).
- [3] M. Nowak and M. Jurczyk, in *Nanotechnology for Energy Sustainability*, edited by B. Raj, r. V. d. Voorde, and Yashwanthajan (Wiley-VCH Verlag GmbH & Co. KGaA, 2017) pp. 433–458.
- [4] J. Liu, S. Han, Y. Li, L. Zhang, Y. Zhao, S. Yang, and B. Liu, *International Journal of Hydrogen Energy* **41**, 20261 (2016).
- [5] Y.-H. Zhang, L.-C. Chen, T. Yang, C. Xu, H.-P. Ren, and D.-L. Zhao, *Rare Metals* **34**, 569 (2015).
- [6] J.-C. Crivello, M. Gupta, and M. Latroche, *Journal of Alloys and Compounds* (2015), 10.1016/j.jallcom.2015.03.177.
- [7] J. Liu, S. Han, D. Han, Y. Li, S. Yang, L. Zhang, and Y. Zhao, *Journal of Power Sources* **287**, 237 (2015).
- [8] L. Zhang, Y. Ding, Y. Li, Y. Zhao, X. Zhao, B. Liu, and S. Han, *Journal of Materials Chemistry A* **4**, 9419 (2016).
- [9] M. Jurczyk, M. Nowak, L. Smardz, and A. Szajek, in *Supplemental Proceedings: Materials Processing and Energy Materials, Volume 1* (John Wiley & Sons, Inc., 2011) pp. 229–236.
- [10] M. Jurczyk, M. Nowak, A. Szajek, and A. Jezierski, *International Journal of Hydrogen Energy* **37**, 3652 (2012).
- [11] M. Balcerzak, M. Nowak, and M. Jurczyk, *International Journal of Hydrogen Energy* **42**, 1436 (2017).
- [12] J.-C. Crivello, J. Zhang, and M. Latroche, *The Journal of Physical Chemistry C* **115**, 25470 (2011).
- [13] M. D. Kuz'min, K. P. Skokov, I. Radulov, C. A. Schwöbel, S. Foro, W. Donner, M. Werwiński, J. Rusz, E. Delczeg-Czirjak, and O. Gutfleisch, *Journal of Applied Physics* **118**, 053905 (2015).
- [14] L. Smardz, K. Smardz, and H. Niedoba, *Journal of Magnetism and Magnetic Materials* **220**, 175 (2000).
- [15] B. E. Deal and C. R. Helms, *The Physics and Chemistry of SiO₂ and the Si-SiO₂ Interface* (Springer Science & Business Media, 2013).
- [16] J. Skoryna, A. Marczyńska, M. Lewandowski, and L. Smardz, *Journal of Alloys and Compounds* (2015), 10.1016/j.jallcom.2014.12.238.
- [17] Y. Baer, G. Busch, and P. Cohn, *Review of Scientific Instruments* **46**, 466 (1975).
- [18] K. Smardz, L. Smardz, I. Okonska, M. Nowak, and M. Jurczyk, *International Journal of Hydrogen Energy IWHE 2006*, **33**, 387 (2008).
- [19] M. Jurczyk, L. Smardz, M. Makowiecka, E. Jankowska, and K. Smardz, *Journal of Physics and Chemistry of Solids* **65**, 545 (2004).
- [20] J. Skoryna, A. Marczyńska, and L. Smardz, *Journal of Alloys and Compounds* **645**, S384 (2015).
- [21] K. Koepnik and H. Eschrig, *Physical Review B* **59**, 1743 (1999).
- [22] K. Koepnik, B. Velický, R. Hayn, and H. Eschrig, *Physical Review B* **55**, 5717 (1997).
- [23] P. Soven, *Physical Review* **156**, 809 (1967).
- [24] J. P. Perdew and Y. Wang, *Physical Review B* **45**, 13244 (1992).
- [25] F. T. Parker and H. Oesterreicher, *Journal of the Less Common Metals* **90**, 127 (1983).
- [26] J. J. Yeh and I. Lindau, *Atomic data and nuclear data tables* **32**, 1 (1985).
- [27] A. P. Pikul, D. Kaczorowski, Z. Gajek, J. Stępień-Damm, A. Ślebarski, M. Werwiński, and A. Szajek, *Physical Review B* **81**, 174408 (2010).
- [28] M. Samsel-Czekala, M. Werwiński, A. Szajek, G. Chełkowska, and R. Troć, *Intermetallics* **19**, 1411 (2011).
- [29] A. V. Virkar and A. Raman, *Journal of the Less Common Metals* **18**, 59 (1969).
- [30] A. Szajek, M. Jurczyk, and W. Rajewski, *Journal of Alloys and Compounds* **307**, 290 (2000).
- [31] V. Yartys, V. Antonov, A. Beskrovnyy, J.-C. Crivello, R. Denys, V. Fedotov, M. Gupta, V. Kulakov, M. Kuzovnikov, M. Latroche, Y. Morozov, S. Sheverev, and B. Tarasov, *Acta Materialia* **82**, 316 (2015).
- [32] P. Aldebert and J. P. Traverse, *Materials Research Bulletin* **14**, 303 (1979).
- [33] E. Levin, P. Donskoy, S. Lushnikov, V. Verbetsky, T. Safonova, and O. Petrii, in *Hydrogen materials science and chemistry of carbon nanomaterials* (Springer, 2004) pp. 503–510.
- [34] F.-L. Zhang, Y.-C. Luo, J.-P. Chen, R.-X. Yan, and J.-H. Chen, *Journal of Alloys and Compounds* **430**, 302 (2007).
- [35] A. Kokalj, *Computational Materials Science* **28**, 155 (2003).
- [36] V. Yartys, A. Riabov, R. Denys, M. Sato, and R. Delaplane, *Journal of Alloys and Compounds* **408-412**, 273 (2006).
- [37] R. V. Denys, A. B. Riabov, V. A. Yartys, M. Sato, and R. G. Delaplane, *Journal of Solid State Chemistry* **181**, 812 (2008).
- [38] M. Dornheim, S. Doppiu, G. Barkhordarian, U. Boesenberg, T. Klassen, O. Gutfleisch, and R. Bormann, *Scripta Materialia Viewpoint set no. 42 “Nanoscale materials for hydrogen storage”*, **56**, 841 (2007).
- [39] Z. Yanghuan, C. Ying, L. Baowei, R. Huiping, H. Zhonghui, and Z. Dongliang, *Rare Metal Materials and Engineering* **42**, 1981 (2013).
- [40] P. C. P. Bouten and A. R. Miedema, *Journal of the Less Common Metals* **71**, 147 (1980).
- [41] R. Griessen and T. Riesterer, in *Hydrogen in Intermetallic Compounds I*, Topics in Applied Physics (Springer, Berlin, Heidelberg, 1988) pp. 219–284.
- [42] L. Smardz, M. Jurczyk, K. Smardz, M. Nowak, M. Makowiecka, and I. Okonska, *Renewable Energy* **33**, 201 (2008).
- [43] T. Liu, Y. Cao, H. Li, W. Chou, and X. Li, *Journal of Power Sources* **267**, 598 (2014).
- [44] Z. Śniadecki, M. Werwiński, A. Szajek, U. K. Röbber, and B. Idzikowski, *Journal of Applied Physics* **115**, 17E129 (2014).
- [45] F. Zhang, Y. Luo, D. Wang, R. Yan, L. Kang, and J. Chen, *Journal of Alloys and Compounds* **439**, 181 (2007).
- [46] L. Smardz, M. Nowak, and M. Jurczyk, *International Journal of Hydrogen Energy* **37**, 3659 (2012).